# Supraparamagnetic, Conductive, and Processable Multifunctional Graphene Nanosheets Coated with High-Density Fe₃O₄ Nanoparticles

**Hongkun He and Chao Gao***

MOE Key Laboratory of Macromolecular Synthesis and Functionalization, Department of Polymer Science and Engineering, Zhejiang University, 38 Zheda Road, Hangzhou 310027, P. R. China

**ABSTRACT** The amazing properties of graphene are triggering extensive interests of both scientists and engineers, whereas how to fully utilize the unique attributes of graphene to construct novel graphene-based composites with tailor-made, integrated functions remains to be a challenge. Here, we report a facile approach to multifunctional iron oxide nanoparticle-attached graphene nanosheets (graphene@$Fe_3O_4$) which show the integrated properties of strong supraparamagnetism, electrical conductivity, highly chemical reactivity, good solubility, and excellent processability. The synthesis method is efficient, scalable, green, and controllable and has the feature of reduction of graphene oxide and formation of $Fe_3O_4$ nanoparticles in one step. When the feed ratios are adjusted, the average diameter of $Fe_3O_4$ nanoparticles (1.2−6.3 nm), the coverage density of $Fe_3O_4$ nanoparticles on graphene nanosheets (5.3−57.9%), and the saturated magnetization of graphene@$Fe_3O_4$ (0.5−44.1 emu/g) can be controlled readily. Because of the good solubility of the as-prepared graphene@$Fe_3O_4$, highly flexible and multifunctional films composed of polyurethane and a high content of graphene@$Fe_3O_4$ (up to 60 wt %) were fabricated by the solution-processing technique. The graphene@$Fe_3O_4$ hybrid sheets showed electrical conductivity of 0.7 S/m and can be aligned into a layered-stacking pattern in an external magnetic field. The versatile graphene@$Fe_3O_4$ nanosheets hold great promise in a wide range of fields, including magnetic resonance imaging, electromagnetic interference shielding, microwave absorbing, and so forth.

**KEYWORDS:** graphene • magnetite • conductivity • nanoparticles • magnetism

## 1. INTRODUCTION

Graphene has been receiving great attention recently due to its unprecedented combination of unique electrical, mechanical, thermal, and optical properties within a single sheet of $sp^2$-bonded carbon atoms (1−6). With the unique two-dimensional (2D) platelike structure and the very high specific surface area (2630 m²/g) (7), graphene could serve as an ideal substrate for the deposition of inorganic nanoparticles (NPs) (8−16). For example, Mülhaupt et al. (8) loaded Pd NPs on graphene nanosheets and applied them as catalysts to the Suzuki-Miyaura coupling reaction. Cao et al. (14) used graphene as an electron-transport matrix to synthesize the graphene-CdS quantum dot nanocomposite and detected a picosecond ultrafast electron transfer process from the excited CdS to graphene by time-resolved fluorescence spectroscopy.

In this regard, magnetic iron oxide (e.g., maghemite $\gamma$-Fe₂O₃ or magnetite Fe₃O₄) NPs have been brought into sharp focus largely due to their magnetic properties, low toxicity, and biocompatibility in physiological environments. Decorating magnetic iron oxide NPs on graphene will impart the desirable magnetic property into graphene, making the composite promising for a variety of fields such as biomedi-

cine, magnetic energy storage, magnetic fluids, catalysis, and environmental remediation (15, 16). Chen et al. (17) deposited Fe₃O₄ NPs onto graphene oxide (GO) by a chemical precipitation method and investigated the binding of the anticancer drug doxorubicin hydrochloride (DXR) on the hybrid for controlled targeted drug delivery. Yu et al. (18) decorated reduced GO sheets with Fe₃O₄ NPs by high-temperature decomposition of the precursor iron(III) acetylacetonate (Fe(acac)₃) and proposed their use as a magnetic resonance contrast agent. Fan et al. (19) reported the attachment of surface-modified Fe₃O₄ NPs to GO by covalent bonding. Ye and co-workers (20) prepared GO loaded with both $\gamma$-Fe₂O₃ and Fe₃O₄−NPs using Fe(acac)₃ in 1-methyl-2-pyrrolidone (NMP) at 190 °C, while Kumar et al. (21) obtained $\alpha$- and $\gamma$-Fe₂O₃ NPs-deposited GO composites at ~150 °C.

Despite the significant efforts, there exist some challenges and problems in the field of graphene/NPs composites: (1) the integrated properties of both graphene and NPs were rarely concerned, (2) the solubility/dispersibility of functionalized graphene nanosheets needs to be improved since the atomic force microscopy (AFM) image of single hybrid sheets has been scarcely reported yet, (3) the composites have rare functional groups for further chemical modification, (4) the preparation protocol is relatively complex, and (5) both size and coverage density of NPs on graphene were hardly controlled.

To resolve such problems, here, we show multifunctional graphene nanosheets attached with magnetite NPs (graphene@$Fe_3O_4$) that integrate both the electrically conductive property of graphene and the superparamagnetism of $Fe_3O_4$ NPs through a facile strategy. Compared with the previous reports, our work shows various advantages. First, the synthesis method of graphene@$Fe_3O_4$ is simple since the reduction of GO to graphene and the in situ formation of $Fe_3O_4$ NPs on graphene sheets are accomplished in a one-step reaction. Second, the surfaces of graphene are evenly covered with uniform $Fe_3O_4$ crystal NPs, and the NPs deposited on graphene sheets are noticeably dense. Third, the growth process of $Fe_3O_4$ NPs on graphene sheets has been traced by transmission electron microscopy (TEM) and AFM observations, showing the mechanism for the dense coverage of NPs on graphene sheets. Fourth, the multifunctional graphene@$Fe_3O_4$ composites possess both the electrically conductive and superparamagnetic properties, and they have good dispersibility in polar solvents and are feasible for solution processing. The combined properties of graphene@$Fe_3O_4$ hold great promise in a wide range of fields, including magnetic separation, biological imaging, aligned substrate for nanodevices, electromagnetic materials and coatings, conducting polymer nanocomposites, and so forth.

## 2. EXPERIMENTAL SECTION

**Materials.** Anhydrous iron(III) chloride ($FeCl_3$, 98%) and diethylene glycol (DEG, 99%) were purchased from Alfa Aesar and used as received. Graphite powder (40 $\mu$m) was obtained from Qingdao Henglide Graphite Co., Ltd. Iron(III) acetylacetonate ($Fe(acac)_3$, Acros, 99%) and palmitoyl chloride (Fluke, 97%) were used as received. NaOH, *N,N*-dimethyl formamide (DMF), and other organic reagents or solvents were obtained from Sinopharm Chemical Reagent Co., Ltd. and used as received.

**Instruments.** Transmission electron microscopy (TEM) analysis was performed on a FEI/Philips CM200 electron microscope operating at 160 kV or a FEI Tecnai G2 F30 S-Twin electron microscope operating at 300 kV. Scanning electron microscopy (SEM) images were obtained on a Hitachi S4800 field-emission SEM system. Atomic force microscopy (AFM) measurements were done using a Digital Instrument Nanoscope IIIa scanning probe microscope, operating at the tapping mode, with samples prepared by spin-coating sample solutions onto freshly cleaved mica substrates at 1500 rpm. The X-ray diffractions (XRD) were recorded on a Philips X'Pert PRO diffractometer equipped with Cu K$\alpha$ radiation (40 kV, 40 mA). X-ray photoelectron spectroscopy (XPS) measurements were performed with a RBD upgraded PHI-5000C ESCA system (Perkin-Elmer) with Mg K$\alpha$ radiation (h$\nu$ = 1253.6 eV) at a power of 250 W. Near-edge X-ray absorption fine structure (NEXAFS) spectroscopy characterizations were performed at the BL08U beamline of Shanghai Synchrotron Radiation Facility (SSRF). Raman spectra were collected on a Jobin-Yvon LabRam HR 800 Raman spectroscope equipped with a 514.5 nm laser source. The magnetic properties were measured using a sample-vibrating magnetometer (VSM, Lake Shore 7410). Thermal gravimetric analysis (TGA) was carried out on a Perkin-Elmer Pyris 6 TGA instrument with a heating rate of 20 °C/min under a nitrogen flow (30 mL/min). Fourier-transform infrared (FTIR) spectra were recorded on a Bruker Vector 22 spectrometer (KBr disk). The electrical conductivities of samples were measured using a Broadband Dielectric spectrometer (Novocontrol Turnkey Concept N40).

**Preparation of GO.** GO was synthesized from natural graphite powder according to the previous resports (22–24), using a modified Hummers method (25, 26) that was originally developed by Kovtyukhova et al. (27). The synthesis procedure consisted of two steps of oxidation. In the first preoxidation step, concentrated $H_2SO_4$ (80 mL) was added into a 500 mL round-bottom flask and heated to 80 °C. $K_2S_2O_8$ (16.8 g) and $P_2O_5$ (16.8 g) were added successively under magnetic stirring. Graphite powder (20 g) was then added slowly into the above solution. The mixture was kept at 80 °C for 4.5 h. After cooling down to room temperature, the mixture was diluted with deionized water and left overnight. Then, the mixture was vacuum-filtered and washed with deionized water (3.2 L) using a 0.22 $\mu$m polycarbonate membrane. The solid was dried under ambient condition for 1 day or longer. In the second oxidation step, a 1 L three-necked round-bottom flask containing 460 mL of concentrated $H_2SO_4$ was chilled to 0 °C in an ethanol-circulated refrigerator equipped with a magnetic stirrer. The preoxidized graphite powder was put into the flask and stirred. Then, $KMnO_4$ (60 g) was added very slowly under continuous stirring, and the temperature was kept below 10 °C. (*Caution*: quickly adding $KMnO_4$ into concentrated $H_2SO_4$ with poor stirring and bad heat transfer may result in highly explosive manganese (VII) oxide.) The mixture was then placed in a water bath at 35 °C and stirred for 2 h. The mixture was then diluted with deionized water (0.92 L) and stirred for 2 h in the ethanol-circulated refrigerator to keep the temperature below 50 °C. Successively, an additional 2.8 L of deionized water was added, followed by addition of 30% $H_2O_2$ (50 mL), causing the color of the mixture to change to bright yellow. The mixture was left undisturbed for 4 days or longer after which the nearly clear supernatant was decanted. The precipitate mixture was put into several 50 mL plastic centrifuge tubes and centrifuged and then washed successively with 1 M HCl solution (at least three centrifugation cycles, centrifugation condition: 10 000 rpm for 3 min) and deionized water (at least five centrifugation cycles, centrifugation condition: 17 500 rpm for longer than 5 min) until the decantate became neutral. The resulting product (GO) was finally stored in deionized water without drying. To determine the concentration of GO in the GO aqueous solution, a certain amount of GO solution was taken and separated by centrifugation, washed with acetone thrice, dried under vacuum at 60 °C overnight, and weighed.

**Preparation of Graphene@$Fe_3O_4$.** Typically, NaOH (200 mg) was added into DEG (20 mL), heated at 120 °C for 1 h in a nitrogen atmosphere, and cooled down to 70 °C to produce a NaOH/DEG stock solution (10 mg NaOH/mL). GO (30 mg) was separated by centrifugation from GO aqueous solution (16 000 rpm, 5 min), redispersed in DEG (20 mL), and sonicated for 1 h. Then, $FeCl_3$ (120 mg) was added and stirred for 1 h. The above mixture was heated to 220 °C for 30 min under the protection of nitrogen flow and constant stirring. A 70 °C NaOH/DEG stock solution (5 mL) was injected rapidly into the above hot mixture. The resulting mixture was further heated at 220 °C for 1 h. The final product of graphene@$Fe_3O_4$ (conditions: the mass feed ratio of $FeCl_3$ to GO ($R_{feed}$-$FeCl_3$) is 4, the mass feed ratio of NaOH to GO ($R_{feed}$-NaOH) is 5/3, the reaction time after addition of NaOH/DEG stock solution is 1 h) was separated by centrifugation and washed with ethanol. The experimental data of different feed ratios are given in Table 1.

**Preparation of Graphene@$Fe_3O_4$–$C_{16}$.** Graphene@$Fe_3O_4$ (2 mg) was dispersed via sonication in 8 mL of dried DMF. After dried triethylamine (0.35 g) and palmitoyl chloride (0.3 g) were added, the reaction was allowed to proceed at 60 °C for 24 h. The product of graphene@$Fe_3O_4$–$C_{16}$ was isolated by centrifugation and rinsed with 1 M HCl, deionized water, and acetone.

**MR Imaging.** Magnetic resonance imaging (MRI) tests were performed on a 1.5 T clinical MRI instrument with a surface coil (Signa Excite HDe, GE Health Care, Milwaukee, WI). Graphene@

**Table 1. Selected Reaction Conditions with Reaction Time of 1 h and Results for the Synthesis of Graphene@Fe$_3$O$_4$ Hybrid Nanosheets**

| $R_{feed}$-FeCl$_3$ | $R_{feed}$-NaOH | GO (mg) | FeCl$_3$ (mg) | NaOH (mg) | $D$ (nm)$^a$ | $C$ (%)$^b$ | $M_s$ (emu/g)$^c$ |
|---|---|---|---|---|---|---|---|
| 0.5 | 5/3 | 30 | 15 | 50 | 5.2 | 13.9 | 0.7 |
| 1 | 5/3 | 30 | 30 | 50 | 5.4 | 24.6 | 5.7 |
| 2 | 5/3 | 30 | 60 | 50 | 6.2 | 35.2 | 30.7 |
| 3 | 5/3 | 30 | 90 | 50 | 6.3 | 47.2 | 44.1 |
| 4 | 5/3 | 30 | 120 | 50 | 6.3 | 57.9 | 42.8 |
| 2 | 1/3 | 30 | 60 | 10 | 1.2 | 5.3 | 0.5 |
| 2 | 1 | 30 | 60 | 30 | 5.9 | 24.7 | 25.0 |
| 2 | 3 | 30 | 60 | 90 | 6.3 | 37.0 | 41.0 |

$^a$ The average diameter of Fe$_3$O$_4$ nanoparticles attached on graphene sheets. $^b$ The coverage density of Fe$_3$O$_4$ nanoparticles on graphene nanosheets (calculated from the ratio of the projective area of nanoparticles on graphene to the area of graphene of corresponding TEM images). $^c$ The saturated magnetization of the graphene@Fe$_3$O$_4$.

Fe$_3$O$_4$ powders (or GO, etc.) were dispersed in a 1% aqueous solution of agarose with various concentrations and then poured into 24-well culture plates (Costar 3524, Corning Inc.) at a volume of 3 mL per well. Agarose was allowed to gel at room temperature. The spaces surrounding each well were full of deionized water to allow appropriate image acquisition. A $T_2$-weighted map was acquired using a spin–echo imaging sequence (TR = 2000 ms; TE = 30, 60, 90, and 120 ms; acquisition matrix = 256 × 256; field of view = 18 × 18 cm; slice thickness = 6 mm; number of averages = 1) (28).

**Preparation of Graphene@Fe$_3$O$_4$/Polyurethane Composites.** Polyurethane was dissolved in DMF to form a 125 mg/mL polyurethane/DMF solution. A certain amount of graphene@Fe$_3$O$_4$ was dispersed in DMF by sonication and mixed with the polyurethane/DMF solution. The mixture was then spread onto a piece of glass, dried in an oven at 60 °C for 48 h, and cooled down to room temperature. The glass was immersed into deionized water to allow the strip to peel off the glass. The strip was clamped between two filtered papers and dried in vacuum at 70 °C for 12 h.

## 3. RESULTS AND DISCUSSION

**One-Pot Synthesis and Characterizations of Graphene@Fe$_3$O$_4$ Hybrid Nanosheets.** To produce soluble graphene-based nanohybrids, graphene is seldom used as a direct starting material, since pure graphene sheets have rare surface functional moieties and poor dispersibility in solvents. Fortunately, graphene oxide (GO) has been proved to be a suitable substitute for graphene, because it possesses lots of oxygen-contained functional groups and can form homogeneous colloidal suspensions in water and polar organic solvents. Also, large-scale preparation of GO is viable by oxidation of natural graphite with strong oxidants. However, GO is electrically insulating (29) and thermally unstable (30), posing a barrier to its applications. Therefore, it is highly needed to convert GO into graphene by reduction via chemical, thermally mediated, or electrochemical methods (31). Although the reduction of GO is feasible, once GO has been incorporated into composites, it is difficult to completely reduce GO to graphene without causing any disruptions to other parts of the composites. Thus, if GO could be reduced during the synthesis process of hybrids or composites, the protocol will be greatly superior.

Generally, three approaches could be used to achieve graphene@Fe$_3$O$_4$ hybrids from GO: (1) first preparation of GO@Fe$_3$O$_4$ following reduction of the product, (2) first reduction of GO and then loading Fe$_3$O$_4$ NPs, and (3) one-pot simultaneous reduction of GO and coating Fe$_3$O$_4$ NPs. The first approach may lead to the detachment of NPs from the nanosheets due to the decomposition of organic linkers during the reduction. As mentioned above, the serious problem associated with the second approach is the aggregation of reduced graphene nanosheets, implying that it is very hard to obtain well dispersed single graphene@Fe$_3$O$_4$ sheets. Besides the poor effect, the two approaches need two pots/steps of reactions, which is adverse for the cost-effective production of the nanohybrids. Herein, we employ the thrid approach to fabricate graphene@Fe$_3$O$_4$ composites via a one-step/pot reaction through a high-temperature solution-phase hydrolysis process (32). The results demonstrated that the one-step approach is superior indeed.

Considering the green process, we selected FeCl$_3$ rather than the generally used Fe(acac)$_3$ as the raw material of iron source. In the reaction, Fe$^{3+}$ ions were first coordinated to the surfaces of GO and then transformed into Fe$_3$O$_4$ NPs in the presence of reducing solvent of DEG with the addition of NaOH at elevated temperature, giving rise to graphene@Fe$_3$O$_4$ hybrid nanosheets. We have done various experiments with different feed ratios of FeCl$_3$ to GO ($R_{feed}$-FeCl$_3$), feed ratios of NaOH to GO ($R_{feed}$-NaOH), or reaction time ($t$) for the synthesis of graphene@Fe$_3$O$_4$. The products have been characterized adequately with various techniques shown below.

As seen in the representative TEM images of graphene@Fe$_3$O$_4$ (Figure 1a–c), the surfaces of graphene are densely covered by narrowly distributed Fe$_3$O$_4$ NPs with average size of 6.3 nm (Figure 1d). The distribution of Fe$_3$O$_4$ NPs on each graphene sheet is even, and no big conglomeration of Fe$_3$O$_4$ NPs or large vacancy on graphene is observed. The lattice fringe spacing (0.25 nm) displayed in the high resolution transmission electron microscopy (HRTEM) image (the inset in Figure 1c) agrees well with the lattice spacing of (311) planes of cubic magnetite.

Figure 2 shows the typical AFM images of single sheets of graphene@Fe$_3$O$_4$ with lateral dimensions of several micrometers. The flat surface of graphene is continuously dotted with protrudent particles without obvious lacuna and has an average thickness of 10–20 nm, which results from
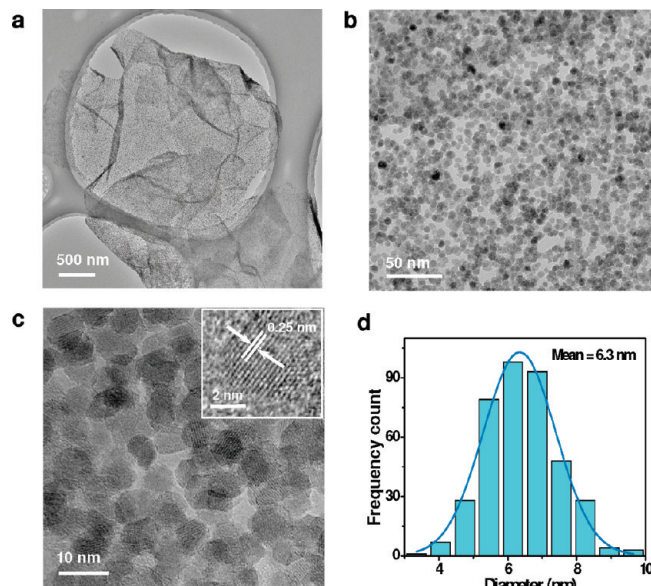
FIGURE 1. TEM images at increasing magnification (a–c) and size distribution analysis of $Fe_3O_4$ nanoparticles (d) of graphene@$Fe_3O_4$ ($R_{feed}$-$FeCl_3$ = 4, $R_{feed}$-NaOH = 5/3, and $t$ = 1 h).
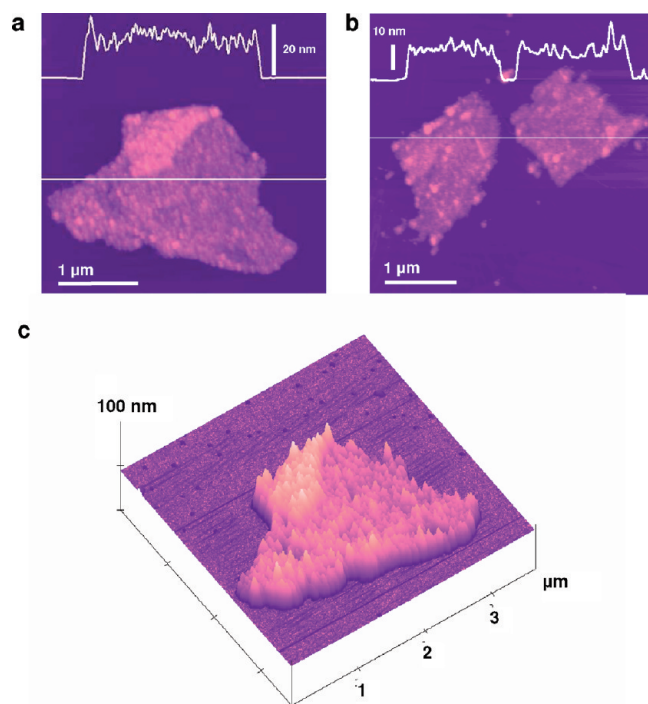


FIGURE 2. AFM images (a, c) of graphene@$Fe_3O_4$ ($R_{feed}$-$FeCl_3$ = 4, $R_{feed}$-NaOH = 5/3, and $t$ = 1 h), and AFM image (b) of graphene@$Fe_3O_4$ ($R_{feed}$-$FeCl_3$ = 2, $R_{feed}$-NaOH = 5/3, $t$ = 15 min).

the fact that both sides of each graphene sheet are coated with $Fe_3O_4$ NPs. AFM images of other graphene@$Fe_3O_4$ samples with different feed ratio or reaction time (see the Supporting Information, Figure S4) show mostly single sheets, suggesting the individual graphene sheets remain isolated after being loaded with $Fe_3O_4$ NPs.

The scanning electron microscopy (SEM) measurements show the thick cakes of graphite (Figure 3a) have been exfoliated into thin large flakes of GO (Figure 3b) after oxidation. In the SEM images of graphene@$Fe_3O_4$ with various feed ratios (Figure 3c–e), the $Fe_3O_4$ NPs appear as
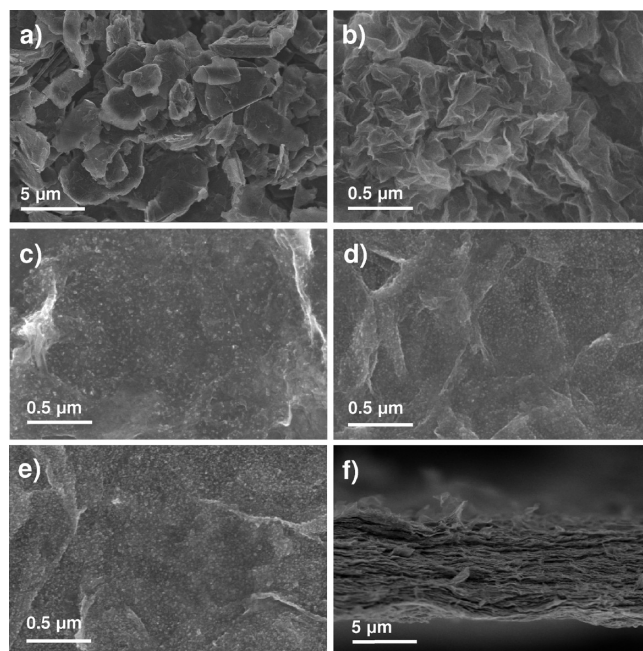


FIGURE 3. SEM top-view images of graphite (a), GO (b), graphene@$Fe_3O_4$ with different $R_{feed}$-$FeCl_3$ ($t$ = 1 h, $R_{feed}$-NaOH = 5/3, $R_{feed}$-$FeCl_3$ = 2 (c), 3 (d), and 4 (e)), and SEM side-view image of a filtered sample of graphene@$Fe_3O_4$ (f).
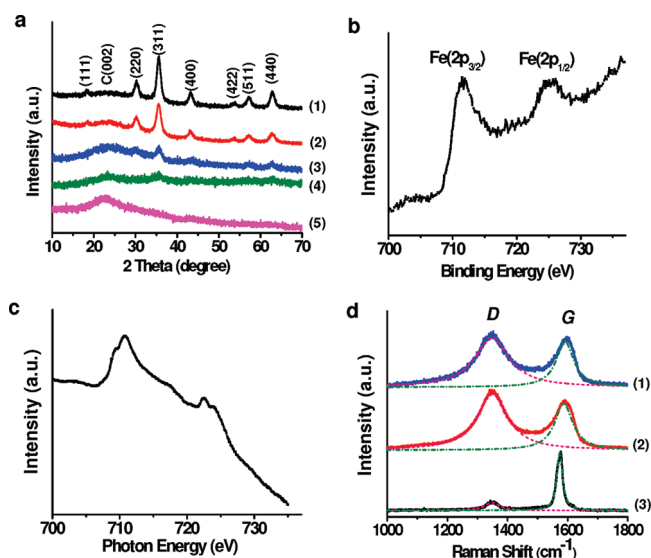


FIGURE 4. (a) XRD patterns of graphene@$Fe_3O_4$ with $R_{feed}$-$FeCl_3$ = 4 (1), 3 (2), 2 (3), 1 (4), and 0.5 (5). (b) The Fe 2p high resolution XPS spectrum of graphene@$Fe_3O_4$. (c) NEXAFS spectrum at Fe L edges of graphene@$Fe_3O_4$. (d) Raman spectra of graphene@$Fe_3O_4$ (1), GO (2), and graphite (3).

bright dots, and the large graphene flakes exhibit a slightly wrinkled surface. The side-view SEM image (Figure 3f) of the cross-sectioned edge of a vacuum filtered graphene@$Fe_3O_4$ film shows a layered structure of thin graphene sheets.

The crystalline structure of $Fe_3O_4$ NPs on graphene was corroborated by XRD measurements. As seen in Figure 4a, the pattern of graphene@$Fe_3O_4$ displayed obvious diffraction peaks of $Fe_3O_4$, and the peak positions and relative intensities match well with the standard XRD data for magnetite (JCPDS card, file No. 19-0629). The broad diffraction peak around 23° corresponds to C(002) reflection of
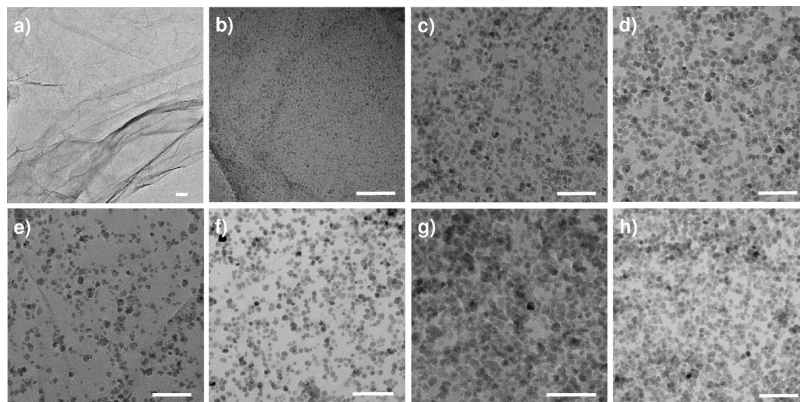
FIGURE 5. TEM images of GO (a), graphene@$Fe_3O_4$ with different $R_{feed}$-NaOH ($t = 1$ h, $R_{feed}$-FeCl$_3$ = 2, $R_{feed}$-NaOH = 1/3 (b), 1 (c), and 3 (d)), and graphene@$Fe_3O_4$ with different $R_{feed}$-FeCl$_3$ ($t = 1$ h, $R_{feed}$-NaOH = 5/3, $R_{feed}$-FeCl$_3$ = 0.5 (e), 1 (f), 2 (g), and 3 (h)). Scale bars, 50 nm.

graphite derived from the short-range order in stacked graphene sheets (12), indicating the reduction of GO in the reaction process (33). With the enlarging of $R_{feed}$-FeCl$_3$, the intensity of $Fe_3O_4$ diffraction peaks become more and more distinct, due to the increasing coverage of $Fe_3O_4$ NPs on graphene. Simultaneously, the C(002) peak gets weakened gradually and cannot be detected for the sample with $R_{feed}$-FeCl$_3$ = 4, indicating that the reduced graphene sheets cannot stack with each other any more to form crystalline structures if the coverage of NPs is densely enough. In other words, individually separated graphene@$Fe_3O_4$ sheets can be obtained in both suspensions and solids.

The X-ray photoelectron spectroscopy (XPS) and near-edge X-ray absorption fine structure (NEXAFS) spectrum were used to further identify the crystal phase of $Fe_3O_4$. In the Fe 2p high resolution XPS spectrum of graphene@$Fe_3O_4$ (Figure 4b), the binding energy peaks at 711.7 and 725.3 eV are corresponding to Fe 2p$_{3/2}$ and Fe 2p$_{1/2}$, respectively, which are very close to the values of $Fe_3O_4$ published in the literature (34). It is noteworthy that the charge transfer satellite of Fe 2p$_{3/2}$ was not detected at around 720 eV, revealing the formation of mixed oxides of Fe(II) and Fe(III) such as $Fe_3O_4$ (35). In the NEXAFS spectrum at the Fe L absorption edges, the splitting of the L$_3$ peak in the region of 705−710 eV and the ratio of two peaks at the L$_2$ edge (719−725 eV) are two important features for distinguishing between $Fe_3O_4$, $\gamma$-$Fe_2O_3$, and $\alpha$-$Fe_2O_3$. For the L$_3$ peak in the region of 705−710 eV in Figure 4c, the splitting was measured to be 1.28 eV, which is close to the value reported in the literature for $Fe_3O_4$ (36). For the two peaks at the L$_2$ edge (719−725 eV) in Figure 4c, the left peak is relatively stronger than the right one, which agrees well with the case reported in the literature for $Fe_3O_4$ (37).

The Raman spectra of graphite, GO, and graphene@$Fe_3O_4$ (Figure 4d) provide the information about the structural changes during the chemical reactions. The G band around 1580 cm$^{-1}$ is related to the in-plane vibration of sp$^2$ carbon atoms in a 2D hexagonal lattice, and the D band around 1350 cm$^{-1}$ is assigned to the vibrations of sp$^3$ carbon atoms of disordered graphite (38). The intensity ratio of the D and G band ($I_D/I_G$) is a useful indicator to evaluate the ordered and disordered crystal structures of carbon. The

value of $I_D/I_G$ is 0.34 for graphite, and it increases to 2.04 for GO, indicating the introduction of many defect sites to GO by the oxidative treatment of graphite. The $I_D/I_G$ for graphene@$Fe_3O_4$ further increases to 2.13 compared with that of GO, which could be attributed to more numerous but smaller sp$^2$ graphitic domains created upon reduction of GO (39) and the presence of some unrepaired defects (40). For comparison, the $I_D/I_G$ values are 1.75 and 2.28 for pure reduced GO samples made by chemical reduction with hydrazine and solvothermal reduction with DEG, respectively (see the Supporting Information, Figure S5).

**Influence of Feed Ratios on the Nanocrystal Growth.** The above characterizations demonstrated the high efficiency of the one-pot approach. To show the controllability and flexibility of this approach, the results of the parallel experiments with different feed ratios and reaction time for the synthesis of graphene@$Fe_3O_4$ were compared. It was found that the amounts of FeCl$_3$ and NaOH added in the synthesis process are the two important factors that influence the average diameter ($D$) of $Fe_3O_4$ NPs, the coverage density ($C$) of $Fe_3O_4$ NPs on graphene nanosheets (calculated from the ratio of the projective area of NPs on graphene to the area of graphene of corresponding TEM images), and the saturated magnetization ($M_s$) of the graphene@$Fe_3O_4$. The TEM images of selected samples are shown in Figure 5, and the corresponding analytical data are shown in Figure 6. As shown in Figure 6a, at fixed $R_{feed}$-FeCl$_3$ = 2 and $t = 1$ h, the $D$, $C$, and $M_s$ increase steadily with increasing $R_{feed}$-NaOH and reach the maximum ($D \sim 6.3$ nm, $C \sim 37.0\%$, $M_s \sim 41.0$ emu/g), because the high alkalinity caused by NaOH favors the quick nucleation and growth of $Fe_3O_4$ (36) (see Figure 5b,c,g,d, and Figure S2 of the Supporting Information). Figure 6c shows that at fixed $R_{feed}$-NaOH = 5/3 and $t = 1$ h, the $D$, $C$, and $M_s$ increase upon increasing $R_{feed}$-FeCl$_3$ and reach the maximum ($D \sim 6.3$ nm, $C \sim 57.9\%$, $M_s \sim 44.1$ emu/g). This is likely due to that the elevated concentration of FeCl$_3$ would accelerate the generation of $Fe_3O_4$ on the graphene substrate and eventually approach a plateau at high $R_{feed}$-FeCl$_3$, which is in coincidence with the TEM observations (see Figures 1, 5e−h, and S1 of the Supporting Information).
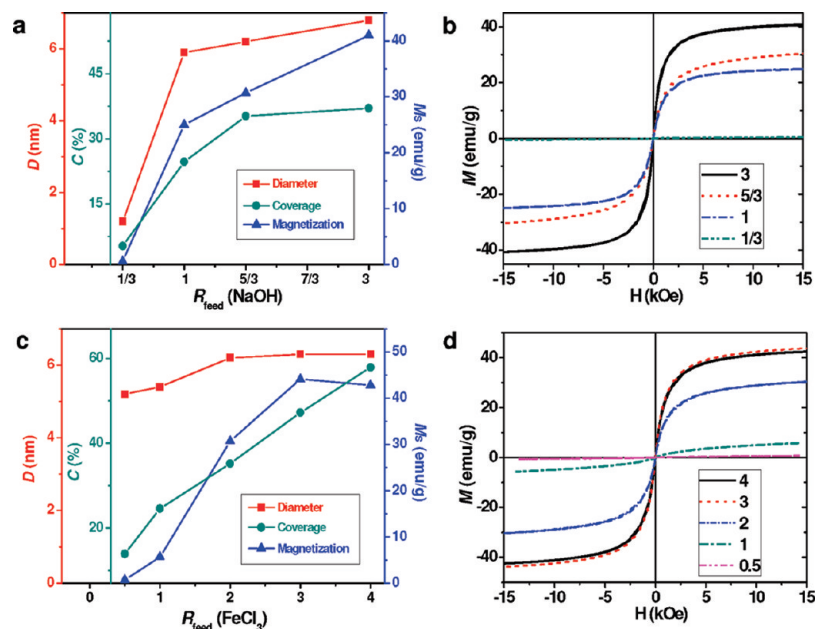
ACS **APPLIED** MATERIALS & INTERFACES

FIGURE 6. Dependence of the average diameter ($D$) of $Fe_3O_4$ nanoparticles, the coverage density ($C$) of $Fe_3O_4$ nanoparticles on graphene nanosheets, and the saturated magnetization ($M_s$) of graphene@$Fe_3O_4$ on $R_{feed}$-NaOH (at fixed $R_{feed}$-FeCl$_3$ = 2 and $t$ = 1 h) (a) and $R_{feed}$-FeCl$_3$ (at fixed $R_{feed}$-NaOH = 5/3 and $t$ = 1 h) (c), respectively. The corresponding magnetic hysteresis loops of (a) and (c) are shown in (b) and (d), respectively.

The obtained data are also listed in Table 1. Generally, $R_{feed}$-FeCl$_3$ has more significant influence on $C$ (13.9−57.9 %) than on $D$ (5.2−6.3 nm); $R_{feed}$-NaOH has strong influence on both $D$ (1.2−6.3 nm) and $C$ (5.3−37.0 %), and both $R_{feed}$-FeCl$_3$ and $R_{feed}$-NaOH have great influence on $M_s$ (0.7−44.1 and 0.5−41.0 emu/g, respectively). It can be concluded that (1) the concentration of FeCl$_3$ primarily determines the formation of $Fe_3O_4$ NPs and, thus, mainly affects their coverage densities, (2) the concentration of NaOH primarily determines the growth rate of $Fe_3O_4$ NPs and, thus, affects their diameters and coverage densities, and (3) both the diameter and coverage density of $Fe_3O_4$ NPs affect the magnetizations of graphene@$Fe_3O_4$. The magnetic hysteresis loops of all these samples (Figure 6b,d) exhibit superparamagnetic characteristics at room temperature with no remanence or coercivity. Consequently, the synthesis strategy allows one to adjust the size of parasitical $Fe_3O_4$ NPs and magnetization of graphene@$Fe_3O_4$ readily in a wide range.

**Kinetics and Mechanism of Graphene-Based Nanocrystal Growth.** A proposed mechanism model for the formation of graphene@$Fe_3O_4$ is shown in Figure 7. With the help of the abundant surface oxygen-containing groups such as carboxyl and hydroxyl, GO is easily suspended in DEG to form a stable colloidal solution by ultrasonication. The iron precursor FeCl$_3$ was then added, and the $Fe^{3+}$ ions were coordinated to the carboxyl groups of GO. Upon increasing the temperature to 220 °C, the color of the reaction mixture turned from light brown to dark brown and then to black, which is a sign that GO has been reduced into graphene (41). The solvothermal reduction of GO in DEG was further confirmed from the Fourier-transform infrared (FTIR) and XRD analyses of the samples obtained in the control experiment in the absence of FeCl$_3$ (see the Supporting Information, Figure S6). Upon the addition of NaOH at high

temperature, $Fe^{3+}$ ions were hydrolyzed to $Fe(OH)_3$ and then partially transformed to $Fe(OH)_2$ under the reductive surrounding and eventually dehydrated to form $Fe_3O_4$ NPs (36).

We traced the growth process of graphene@$Fe_3O_4$ by offline TEM observations of a series of samples that are taken out from the reaction system at different times. The TEM analysis (see the inset in Figure 7 and Figure S3 of the Supporting Information) reveals that the formation of $Fe_3O_4$ nanocrystals on graphene was a dynamic process that follows the classic La Mer model (42). In the initial nucleation stage, a temporally discrete nucleation occurred immediately upon the rapid injection of NaOH solution. The high reaction temperature greatly accelerates the nucleation process, leading to the burst of nucleation within several seconds. The quick nucleation helps to obtain magnetite nanocrystals with relatively narrow size distributions (43). In the next growth stage, the nuclei formed in the initial stage quickly grow to larger crystals during the first 5 min after nucleation. The average particle sizes are around 1.6, 3.1, 4.0, 4.4, 4.6, and 4.8 nm at 0, 1, 2, 3, 4, and 5 min, respectively. According to the Lifshitz−Slyozov−Wagner (LSW) theory for Ostwald ripening, for a system of highly dispersed particles with the diffusion-controlled growth, the rate law is given by

$$\bar{r}^3 - \bar{r}_0{}^3 = Kt \tag{1}$$

$$K = \frac{8\gamma D V_m{}^2 C_\infty}{9RT} \tag{2}$$

where $\bar{r}$ is the mean particle radius at time $t$, $\bar{r}_0$ is the initial particle radius at time zero, $C_\infty$ is the equilibrium concentra-
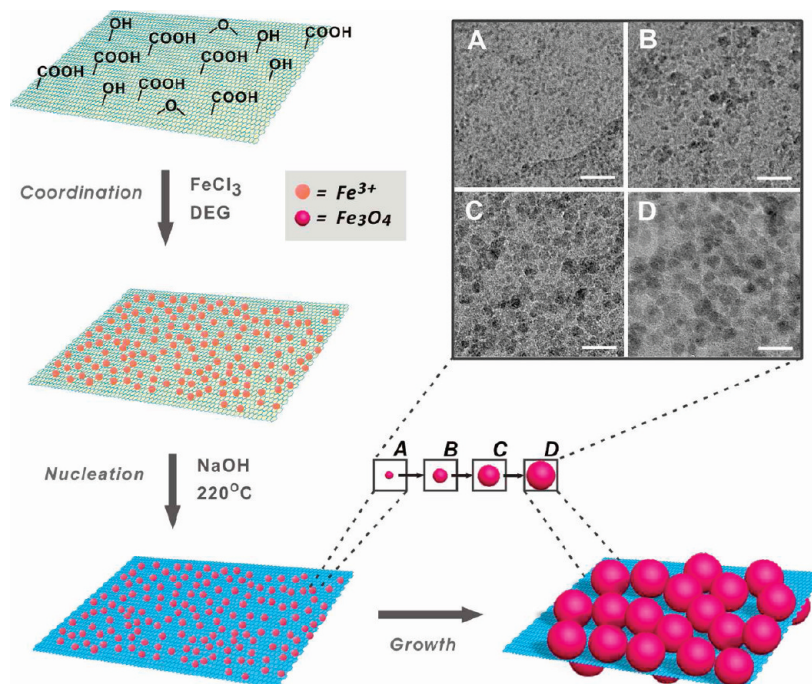
**FIGURE 7. Schematic illustration of the formation of graphene@Fe₃O₄.** The inset shows the TEM images of graphene@Fe₃O₄ at reaction time of 0 (A), 1 (B), 5 (C), and 60 min (D). Scale bars, 20 nm.

tion at a flat surface, $\gamma$ is the interfacial energy, $V_m$ is the molar volume of the solid phase, $R$ is the gas constant, and $T$ is the temperature (44). When the experimental data is fitted into eq 1 (see the inset in Figure 8a), the constant $K$ is calculated to be 21.6 (nm³/min). The growth kinetics of Fe₃O₄ particles follows the Ostwald ripening, in which smaller particles dissolve owing to their high surface energy and are essentially consumed by larger ones (42). After 5 min, the increase of Fe₃O₄ particle size is very slow (5.3, 5.5, 5.9, and 6.2 nm at 10, 15, 30, and 60 min, respectively), and even a 24 h of growth only leads to a particle size of 6.8 nm. The magnetic hysteresis loops of the samples obtained at different reaction times (Figure 8b) show superparamagnetic behaviors, and the change of $M_s$ (Figure 8a) shows the similar tendency to that of a particle size increase, that is, fast increase within the first few minutes and very slow increase after that (approaching 36.1 emu/g at 24 h).

The NPs supported on graphene sheets reported herein are remarkably dense compared with those in other reported cases of inorganic particles (8–16), presumably due to the different synthesis methods. In our cases, the process of high-temperature solution-phase hydrolysis allows the instantaneous nucleation and quick growth of Fe₃O₄ particles. In order to verify this supposition, we conducted control experiments to synthesize Fe₃O₄ NPs on GO via a commonly used high-temperature decomposition method using Fe(acac)₃ as the precursor. The formation of Fe₃O₄ NPs resulted from the decomposition of Fe(acac)₃ is a slow process, leading to graphene sheets relatively sparsely decorated with Fe₃O₄ NPs with coverage density of around 14.0 % (see Figure 9a and Figure S7 of the Supporting Information). In addition, control experiments using highly reduced graphene oxide (HRG) (45) as the starting material were also conducted, but only very few Fe₃O₄ NPs were observed on

the HRG sheets in the TEM image (Figure 9b). This is because the oxygen-containing functional groups are almost entirely removed from GO by hydrazine in the preparation of HRG, and Fe³⁺ ions could not coordinate to the surfaces of HRG sheets. The control experiments in turn affirm the necessity of the use of multifunctional GO instead of graphene or HRG as the starting material. Furthermore, it is noteworthy that the existence of carboxyl groups of GO is an essential prerequisite for the formation of Fe₃O₄ NPs on graphene sheets, which are confirmed by the following two control experiments. The chemically modified graphene containing carboxyl moiety can also produce graphene@Fe₃O₄, whereas Fe₃O₄ NPs cannot deposit on the chemically modified graphene containing hydroxyl moiety (see Figures 9c,d and S8 of the Supporting Information).

**Solubility and Multifunctionality of Graphene@Fe₃O₄ Nanosheets.** It is known that pure graphene and reduced GO without any modification tend to aggregate and could not disperse in most solvents due to the lack of surface moieties (46), which seriously limits their applications (47). Interestingly, our graphene@Fe₃O₄ hybrids could be dispersed by sonication in many polar solvents such as ethanol, water, and DMF (Figure 10a). Two main factors are responsible for the improved solubility of graphene@Fe₃O₄ as compared to graphene. For one thing, the deposited Fe₃O₄ NPs could prevent graphene sheets from severe aggregation during the reduction of GO. The same phenomenon was also found in the case of platinum NPs deposited on graphene (12). For another, the polyol solvent of DEG can attach to the surfaces of graphene@Fe₃O₄ as ligand of NPs after reaction, and enhance the dispersibility of product in polar solvents accordingly. The presence of DEG on graphene@Fe₃O₄ is confirmed by the thermal gravimetric analysis (TGA)
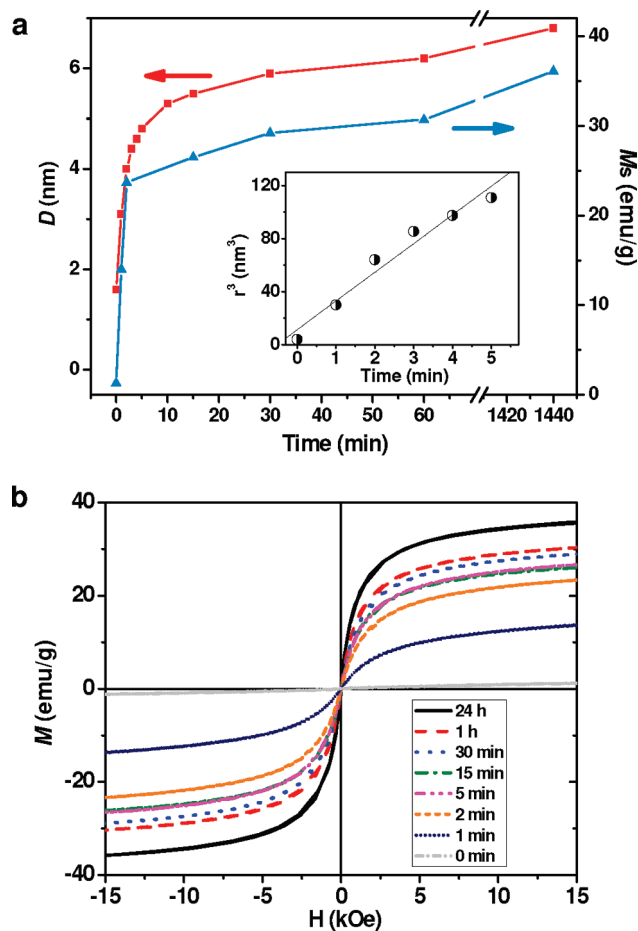
**FIGURE 8.** (a) Dependence of the average diameter ($D$) of $Fe_3O_4$ nanoparticles and the saturated magnetization ($M_s$) of graphene@$Fe_3O_4$ on reaction time. The inset shows the cube of average particle radius of $Fe_3O_4$ nanoparticles on graphene versus the growth time. The fitting line accords with the LSW model. (b) The corresponding magnetic hysteresis loops of (a).

**FIGURE 9.** TEM images of the samples from the control experiments for graphene@$Fe_3O_4$: (a) using Fe(acac)$_3$ instead of FeCl$_3$/NaOH, (b) using highly reduced graphene oxide (HRG) instead of GO, (c) using chemically modified graphene with hydroxyl moiety instead of GO, and (d) using chemically modified graphene with carboxyl moiety instead of GO.
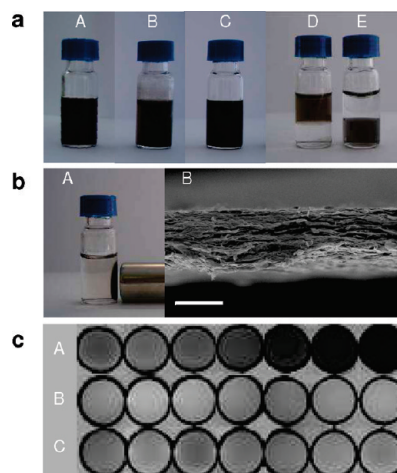


**FIGURE 10.** (a) Photographs of 1.5 mg/mL graphene@$Fe_3O_4$ dispersion in ethanol (A), water (B), and DMF (C) after sonication. The photographs of graphene@$Fe_3O_4$ (D) and graphene@$Fe_3O_4$–$C_{16}$ (E) dispersed in water/chloroform. (b) The photograph of graphene@$Fe_3O_4$ in DMF separated by a magnet (A), and SEM side-view image of graphene@$Fe_3O_4$ dried in an external magnetic field (B). Scale bar, 5 $\mu$m. (c) $T_2$-weighted MR imaging of graphene@$Fe_3O_4$ (A), HRG (B), and GO (C) at different concentrations (from left to right in each row: 0, 6.25, 12.5, 25, 50, 100, and 200 $\mu$g/mL).

and FTIR analyses of the graphene@$Fe_3O_4$ sample (see the Supporting Information, Figure S9). About 20 wt % weight loss between 230 and 500 °C was found in the TGA curve of graphene@$Fe_3O_4$, suggesting the high density coating of DEG on the NP surfaces. XPS measurements showed that the elemental contents of Fe, O, and C for the sample of graphene@$Fe_3O_4$ ($t$ = 1 h, $R_{feed}$-NaOH = 5/3, $R_{feed}$-FeCl$_3$ = 4) were 8.66, 32.15, and 59.19 %, respectively. According to the atom ratio, the $Fe_3O_4$ weight percent is calculated to be around 39.2 %. Obviously, the extra-high oxygen content can be mainly attributed to the attachment of DEG molecules, which is in agreement with the TGA result. Such a high content of $Fe_3O_4$ NPs results in the strong $M_s$s (>40 emu/g) of our graphene@$Fe_3O_4$ samples. The $M_s$ of the control sample made from Fe(acac)$_3$ is less than 10 emu/g (9.4 emu/g) due to the relatively low coverage/content of $Fe_3O_4$ NPs (Supporting Information Figure S7A). As a comparison, Kumar and co-workers reported that the maximum $M_s$ of their magnetic samples made from Fe(acac)$_3$ is only 5.5 emu/g.

Furthermore, the hydroxyl groups of DEG on the graphene@$Fe_3O_4$ were utilized to react with palmitoyl chloride to produce long alky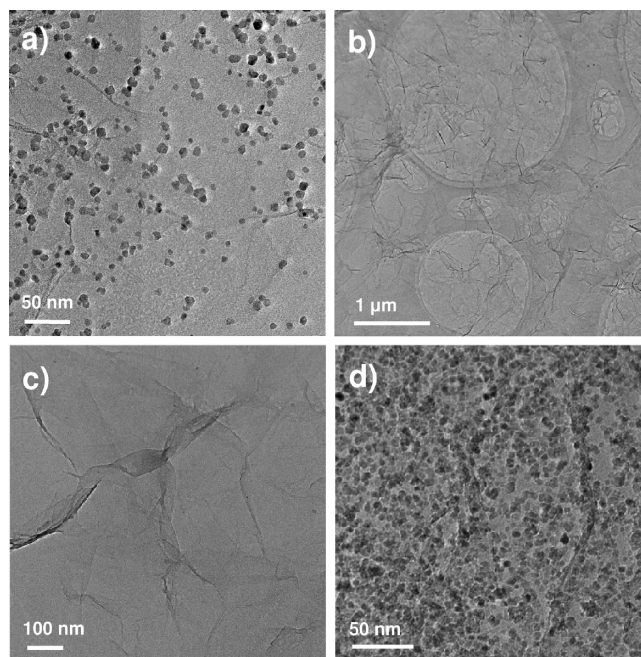l chain-modified graphene@$Fe_3O_4$ (graphene@$Fe_3O_4$–$C_{16}$), resulting in the change of surface property from hydrophilic to hydrophobic. When placed in the water/chloroform mixture, the graphene@$Fe_3O_4$ dispersed in the upper layer of polar water, whereas graphene@$Fe_3O_4$–$C_{16}$ transferred to the lower layer of nonpolar chloroform (Figure 10a), suggesting the successful surface modification. The highly reactive platform of multi-hydroxyl graphene@$Fe_3O_4$ lays the foundation for introduc-
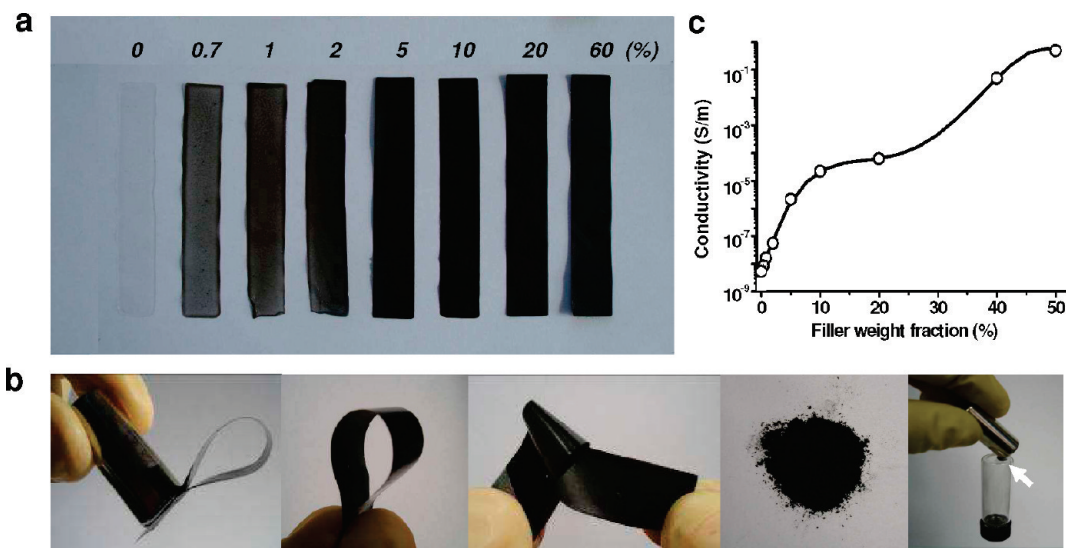
FIGURE 11. (a) Photographs of ~40 μm thick strips of graphene@$Fe_3O_4$−polyurethane composites with different filler contents. (b) From left to right: the photographs of a strip of graphene@$Fe_3O_4$−polyurethane composites (50 wt %) lifted with a magnet, held and twisted with hands, dried graphene@$Fe_3O_4$ powder, and 6.0 mg of graphene@$Fe_3O_4$ powder that can lift a 5.05 g glass bottle with a magnet, respectively. (c) Electrical conductivity of graphene@$Fe_3O_4$−polyurethane composites as a function of filler weight fraction.

ing other functional compositions and desired moieties with tailor-made properties by chemical modification.

**Magnetic Alignment and MR Imaging.** The strong superparamagnetic attribute of graphene@$Fe_3O_4$ offers significant use for biomagnetic separations, as the carriers for targeted drug delivery and as the contrast agents in magnetic resonance imaging (MRI). The magnetic components of graphene@$Fe_3O_4$ render mobility under an external magnetic field. When a magnet is placed beside a bottle filled with graphene@$Fe_3O_4$ dispersed in DMF, the graphene@$Fe_3O_4$ particles quickly move along the magnetic field and completely deposit near the magnet (Figure 10b). SEM observations on the graphene@$Fe_3O_4$ sheets that were separated from the solvent and dried in an external magnetic field showed an aligned layered-stacking pattern (Figure 10b), which is very similar to the vacuum-filtered samples as shown in Figure 2f. Such an example of magnetically induced self-assembly indicates that the water-soluble graphene@$Fe_3O_4$ could be used in the magnetic array and cell manipulation (48). This result also demonstrates that large-area aligned graphene nanosheets can be produced via magnetic force, which would be a breakthrough for the fabrication of graphene-based electromagnetic devices, transistors, and displays, as aligned carbon nanotubes have shown (49).

Moreover, since the magnetic iron oxide NPs are now established as MRI contrast agents in current MRI techniques, we also performed MRI experiments on a 1.5 T clinical imaging system to test the feasibility of the use of the superparamagnetic graphene@$Fe_3O_4$ as a novel contrast agent. The $T_2$-weight MR imaging of graphene@$Fe_3O_4$ shows strong MR relaxation enhancement (Figure 10c), promising its potential in MRI technology. As a comparison, no enhancement was observed for the samples containing neat GO or HRG.

**Conductive and Magnetic Polymer Composites of Graphene@$Fe_3O_4$.** The electrical conductivity is a pivotal property of graphene. Chemical treatment could improve its solubility but also may destroy the structure of graphene, usually leading to the vanishing of conductivity. Therefore, a big question appears: is the graphene@$Fe_3O_4$ still conductive? To our delight, the graphene@$Fe_3O_4$ film made by vacuum-filtering was demonstrated to be electrically conductive (~0.7 S/m). The insulative GO has been reduced to graphene via solvothermal reduction and restored the conductivity by recovering the conjugated network (40). Due to the obstruction of $Fe_3O_4$ NPs between the basal planes of graphene nanosheets, the conductivity of graphene@$Fe_3O_4$ is lower than that of HRG or modified graphene paper samples (in the range of $10^2-10^4$ S/m) (45).

The solubility and versatility of the graphene@$Fe_3O_4$ sheets pave the way for the fabrication of multifunctional composites by the convenient solution-processing technique. Herein, we produced various graphene@$Fe_3O_4$-polymer films by solution-phase mixing of graphene@$Fe_3O_4$ with polyurethane elastomer. The colors of the resulting films turn gradually from transparent to black upon the content of graphene@$Fe_3O_4$ raised from 0 to 60 wt % (Figure 11a). The composite films have evident magnetic response to an external field and excellent flexibility (Figure 11b). Significantly, the film loaded with nanofillers of graphene@$Fe_3O_4$ as high as 50 wt % is also quite flexible and can be folded without fissuring. The electrical conductivity of the graphene@$Fe_3O_4$−polyurethane composites is shown in Figure 11c. The conductivity values of the graphene@$Fe_3O_4$−polyurethane composites are comparable with those of graphene−polymer composites reported in the literature (50). Therefore, the multifunctional graphene@$Fe_3O_4$ could serve as a new kind of promising nanofiller to produce high-performance polymer composites and coatings with both electrical and magnetic properties, which are greatly useful in electromagnetic interference (EMI) shielding, microwave absorbing, flexible electronics materials, etc (51, 52).

## 4. CONCLUSIONS

In summary, we have demonstrated a facile and efficient chemical approach to prepare multifunctional nanosheets of graphene@$Fe_3O_4$ with scalable, cost-effective, highly reproducible, and well controllable merits. With $Fe_3O_4$ NPs densely coated on the surfaces of graphene, the superparamagnetic and conductive properties are integrated into individual nanosheets, making multifunctional single-sheet nanohybrids practicable. The graphene@$Fe_3O_4$ nanosheets can be aligned as large-area layered-stacking films with a magnetically controlled methodology, opening the avenue to extraordinary nanoelectronic devices and materials made of graphene. The graphene@$Fe_3O_4$ nanocomposites are readily processable in solvents, facilitating their versatile applications. The multihydroxyl groups associated with the $Fe_3O_4$ NPs enable the graphene@$Fe_3O_4$ highly reactive, affording a 2D nanoplatform for construction of desirable bionano conjugates via a chemical approach. Our finding can be extended to different kinds of multifunctional graphene-based nanocomposites, paving the way for the extensive exploration of graphene with fascinating functionalities. In addition, because of the extremely dense coverage of $Fe_3O_4$ on the graphene template, the graphene@$Fe_3O_4$ could play the role of precursor of iron oxide nanosheets or iron oxidene, casting an optimistic light for achieving other quantum planes built with noncarbon atoms, molecules, or NPs.

**Supporting Information Available:** Additional TEM and AFM images, Raman spectra, photographs, TGA, FTIR, and XRD data. This material is available free of charge via the Internet at http://pubs.acs.org.

## REFERENCES AND NOTES

(1) Park, S.; Ruoff, R. S. *Nat. Nanotechnol.* **2009**, *4*, 217–224.
(2) Rao, C. N. R.; Sood, A. K.; Subrahmanyam, K. S.; Govindaraj, A. *Angew. Chem., Int. Ed.* **2009**, *48*, 7752–7777.
(3) Geim, A. K. *Science* **2009**, *324*, 1530–1534.
(4) Geim, A. K.; Novoselov, K. S. *Nat. Mater.* **2007**, *6*, 183–191.
(5) Katsnelson, M. I. *Mater. Today* **2007**, *10*, 20–27.
(6) Loh, K. P.; Bao, Q.; Ang, P. K.; Yang, J. *J. Mater. Chem.* **2010**, *20*, 2277.
(7) Stoller, M. D.; Park, S. J.; Zhu, Y. W.; An, J. H.; Ruoff, R. S. *Nano Lett.* **2008**, *8*, 3498–3502.
(8) Scheuermann, G. M.; Rumi, L.; Steurer, P.; Bannwarth, W.; Mülhaupt, R. *J. Am. Chem. Soc.* **2009**, *131*, 8262–8270.
(9) Muszynski, R.; Seger, B.; Kamat, P. V. *J. Phys. Chem. C* **2008**, *112*, 5263–5266.
(10) Goncalves, G.; Marques, P.; Granadeiro, C. M.; Nogueira, H. I. S.; Singh, M. K.; Gracio, J. *Chem. Mater.* **2009**, *21*, 4796–4802.
(11) Xu, C.; Wang, X.; Zhu, J. W. *J. Phys. Chem. C* **2008**, *112*, 19841–19845.
(12) Si, Y. C.; Samulski, E. T. *Chem. Mater.* **2008**, *20*, 6792–6797.
(13) Pasricha, R.; Gupta, S.; Srivastava, A. K. *Small* **2009**, *5*, 2253–2259.
(14) Cao, A.; Liu, Z.; Chu, S.; Wu, M.; Ye, Z.; Cai, Z.; Chang, Y.; Wang, S.; Gong, Q.; Liu, Y. *Adv. Mater.* **2009**, *21*, 103–106.
(15) Lu, A. H.; Salabas, E. L.; Schuth, F. *Angew. Chem., Int. Ed.* **2007**, *46*, 1222–1244.
(16) Frey, N. A.; Peng, S.; Cheng, K.; Sun, S. H. *Chem. Soc. Rev.* **2009**, *38*, 2532–2542.
(17) Yang, X. Y.; Zhang, X. Y.; Ma, Y. F.; Huang, Y.; Wang, Y. S.; Chen, Y. S. *J. Mater. Chem.* **2009**, *19*, 2710–2714.
(18) Cong, H. P.; He, J. J.; Lu, Y.; Yu, S. H. *Small* **2009**, *6*, 169–173.
(19) He, F.; Fan, J.; Ma, D.; Zhang, L.; Leung, C.; Chan, H. L. *Carbon* **2010**, *48*, 3139–3144.
(20) Shen, J. F.; Hu, Y. Z.; Shi, M.; Li, N.; Ma, H. W.; Ye, M. X. *J. Phys. Chem. C* **2010**, *114*, 1498–1503.
(21) Singh, V. K.; Patra, M. K.; Manoth, M.; Gowd, G. S.; Vadera, S. R.; Kumar, N. *New Carbon Mater.* **2009**, *24*, 147–152.
(22) Xu, Z.; Gao, C. *Macromolecules* **2010**, *43*, 6716–6723.
(23) He, H. K.; Gao, C. *Chem. Mater.* **2010**, *22*, 5054–5064.
(24) Kou, L.; He, H. K.; Gao, C. *Nano-Micro Lett.* **2010**, *2*, 177–183.
(25) Tung, V. C.; Allen, M. J.; Yang, Y.; Kaner, R. B. *Nat. Nanotechnol.* **2009**, *4*, 25–29.
(26) Hummers, W. S.; Offeman, R. E. *J. Am. Chem. Soc.* **1958**, *80*, 1339–1339.
(27) Kovtyukhova, N. I.; Ollivier, P. J.; Martin, B. R.; Mallouk, T. E.; Chizhik, S. A.; Buzaneva, E. V.; Gorchinskiy, A. D. *Chem. Mater.* **1999**, *11*, 771–778.
(28) Wan, J.; Cai, W.; Meng, X.; Liu, E. *Chem. Commun.* **2007**, 5004–5006.
(29) Jung, I.; Pelton, M.; Piner, R.; Dikin, D. A.; Stankovich, S.; Watcharotone, S.; Hausner, M.; Ruoff, R. S. *Nano Lett.* **2007**, *7*, 3569–3575.
(30) Lambert, T. N.; Chavez, C. A.; Hernandez-Sanchez, B.; Lu, P.; Bell, N. S.; Ambrosini, A.; Friedman, T.; Boyle, T. J.; Wheeler, D. R.; Huber, D. L. *J. Phys. Chem. C* **2009**, *113*, 19812–19823.
(31) Dreyer, D. R.; Park, S.; Bielawski, C. W.; Ruoff, R. S. *Chem. Soc. Rev.* **2010**, *39*, 228–240.
(32) Ge, J. P.; Hu, Y. X.; Biasini, M.; Beyermann, W. P.; Yin, Y. D. *Angew. Chem., Int. Ed.* **2007**, *46*, 4342–4345.
(33) Nethravathi, C.; Rajamathi, M. *Carbon* **2008**, *46*, 1994–1998.
(34) Teng, X. W.; Black, D.; Watkins, N. J.; Gao, Y. L.; Yang, H. *Nano Lett.* **2003**, *3*, 261–264.
(35) Morel, A. L.; Nikitenko, S. I.; Gionnet, K.; Wattiaux, A.; Lai-Kee-Him, J.; Labrugere, C.; Chevalier, B.; Deleris, G.; Petibois, C.; Brisson, A.; Simonoff, M. *ACS Nano* **2008**, *2*, 847–856.
(36) Ge, J. P.; Hu, Y. X.; Biasini, M.; Dong, C. L.; Guo, J. H.; Beyermann, W. P.; Yin, Y. D. *Chem.—Eur. J.* **2007**, *13*, 7153–7161.
(37) Sun, S. H.; Zeng, H.; Robinson, D. B.; Raoux, S.; Rice, P. M.; Wang, S. X.; Li, G. X. *J. Am. Chem. Soc.* **2004**, *126*, 273–279.
(38) Zhang, W. X.; Cui, J. C.; Tao, C. A.; Wu, Y. G.; Li, Z. P.; Ma, L.; Wen, Y. Q.; Li, G. T. *Angew. Chem., Int. Ed.* **2009**, *48*, 5864–5868.
(39) Stankovich, S.; Dikin, D. A.; Piner, R. D.; Kohlhaas, K. A.; Kleinhammes, A.; Jia, Y.; Wu, Y.; Nguyen, S. T.; Ruoff, R. S. *Carbon* **2007**, *45*, 1558–1565.
(40) Zhou, Y.; Bao, Q. L.; Tang, L. A. L.; Zhong, Y. L.; Loh, K. P. *Chem. Mater.* **2009**, *21*, 2950–2956.
(41) Williams, G.; Seger, B.; Kamat, P. V. *ACS Nano* **2008**, *2*, 1487–1491.
(42) Murray, C. B.; Kagan, C. R.; Bawendi, M. G. *Annu. Rev. Mater. Sci.* **2000**, *30*, 545–610.
(43) Yin, Y.; Alivisatos, A. P. *Nature* **2005**, *437*, 664–670.
(44) Wong, E. M.; Bonevich, J. E.; Searson, P. C. *J. Phys. Chem. B* **1998**, *102*, 7770–7775.
(45) Park, S.; An, J. H.; Jung, I. W.; Piner, R. D.; An, S. J.; Li, X. S.; Velamakanni, A.; Ruoff, R. S. *Nano Lett.* **2009**, *9*, 1593–1597.
(46) Li, D.; Muller, M. B.; Gilje, S.; Kaner, R. B.; Wallace, G. G. *Nat. Nanotechnol.* **2008**, *3*, 101–105.
(47) Ruoff, R. S. *Nat. Nanotechnol.* **2008**, *3*, 10–11.
(48) Gao, C.; Li, W.; Morimoto, H.; Nagaoka, Y.; Maekawa, T. *J. Phys. Chem. B* **2006**, *110*, 7213–7220.
(49) Terrones, M.; Grobert, N.; Olivares, J.; Zhang, J. P.; Terrones, H.; Kordatos, K.; Hsu, W. K.; Hare, J. P.; Townsend, P. D.; Prassides, K.; Cheetham, A. K.; Kroto, H. W.; Walton, D. R. M. *Nature* **1997**, *388*, 52–55.
(50) Stankovich, S.; Dikin, D. A.; Dommett, G. H. B.; Kohlhaas, K. M.; Zimney, E. J.; Stach, E. A.; Piner, R. D.; Nguyen, S. T.; Ruoff, R. S. *Nature* **2006**, *442*, 282–286.
(51) Qiu, G. H.; Wang, Q.; Nie, M. *J. Appl. Polym. Sci.* **2006**, *102*, 2107–2111.
(52) Gas, J.; Poddar, P.; Almand, J.; Srinath, S.; Srikanth, H. *Adv. Funct. Mater.* **2006**, *16*, 71–75.

AM100673G